



Electrochemical performance evaluation of carbon nitride synthesized at different temperatures as an anode material for lithium-ion batteries

Gnanavel Angamuthu¹ · Ezhilan Jayabal¹ · Venkatesan Rengarajan¹

Received: 29 October 2019 / Revised: 14 February 2020 / Accepted: 5 April 2020 / Published online: 14 May 2020
© Springer-Verlag GmbH Germany, part of Springer Nature 2020

Abstract

Carbon nitride has limited application in lithium-ion batteries (LIB) due to the deterioration of its crystallinity, difficulties in lithium-ion intercalation/de-intercalation, and poor capacity and cyclic stability. To overcome the above-mentioned issues, we have synthesized carbon nitride at different temperatures and evaluated its electrochemical performance as an anode material. The results demonstrated that the carbon nitride synthesized at 600 °C (C_3N_4 —600 °C) delivers a remarkable specific capacity 2221 mAh g⁻¹ at 0.1C-rate, with enhanced rate capability and cycling stability. The enhanced electrochemical performances may promote the utilization of carbon nitride in energy storage devices.

Keywords Carbon nitride (C_3N_4) · Elevated temperature · Anode material · High lithium storage · Enhanced kinetics · Electrochemical active porous site · Lithium-ion battery

Introduction

Lithium-ion battery (LIB) enters the green energy storage technology and is suitable for consumer electronics. However, the growth of LIB technology is retarded by many parameters such as damages caused by stress-induced materials. The growth of solid electrolyte interface (SEI) enhances interfacial resistance due to unwanted side reaction, low capacity, volume expansion, and slow kinetics [1–6]. To address these issues, the active research relies much on the development of safe, low-cost, and reliable efficient electrode and electrolyte. So, here, we are interested to develop an anode material for the LIB. Many efforts have been taken by various research groups to develop a suitable anode for LIB technology. The anodes based on alloy/de-alloying materials such as Si (theoretical capacity, 4212 mAh g⁻¹) [7], Ge (theoretical

capacity, 1624 mAh g⁻¹) [8], Sn (theoretical capacity, 993 mAh g⁻¹) [9], Sb (theoretical capacity, 660 mAh g⁻¹) [10], SnO₂ (theoretical capacity, 790 mAh g⁻¹) [11], and SiO (theoretical capacity, 1600 mAh g⁻¹) [12] yield large capacity and high energy density, but the main concern is that when the lithium reacts with active material, it leads to huge volume expansion which is the main cause for the low capacity, coulombic efficiency, and unstable solid electrolyte interface (SEI) [13]. Further, some of the research groups aimed at the intercalation/de-intercalation-based materials such as carbonaceous (carbonaceous, 200–600 mAh g⁻¹; hard carbon, 1116 mAh g⁻¹; CNT, 780/1116 mAh g⁻¹) [14–19] and titanium oxide materials (LiTi₄O₅, 175 mAh g⁻¹; TiO₂, 330 mAh g⁻¹) [20]. The developed material's storage capacity majorly depends on the intercalation/de-intercalation process and material's surface area and crystallinity. The titanium-oxide-based material possesses high reversible capacity, power density, and safety which makes it a suitable candidate, but still due to its poor energy density, the production cost is a major concern. Also, metal oxide-based materials such as Fe₂O₃, Fe₃O₄, CoO, Co₃O₄, Mn_xO_x, Cu₂O/CuO, NiO, Cr₂O₃, RuO₂, and MoO₃/MoO₃ have been developed and the theoretical capacity of these materials falls between the range 500 to 1200 mAh g⁻¹. Also, the transition metal-based

Electronic supplementary material The online version of this article (<https://doi.org/10.1007/s11581-020-03566-w>) contains supplementary material, which is available to authorized users.

✉ Venkatesan Rengarajan
venkatesanr.che@pondiuni.edu.in; venkatesanrpu@gmail.com

¹ Department of Chemistry, Pondicherry University,
Pondicherry 605014, India

phosphides, nitrides, and sulfides were developed and these materials exhibit the capacity of 500 to 1800 mAh g⁻¹ having drawbacks such as large potential hysteresis and unstable SEI formation, making it a less utilizable LIB technology [21–23]. Furthermore, the current LIB technology employs graphite-based anodes with theoretical capacity of 372 mAh g⁻¹ but due to its poor active sites results in slow kinetics [24–26]. In addition to that, the nitrogen-doped graphite and graphene had been developed, which delivers a superior rate capability and high capacity than the bare graphite [27–35]. So, the researchers were in search of carbon and nitrogen-containing material and found that graphitic carbon nitride possesses high nitrogen content: three types of nitrogen graphitic, pyridinic, and bridged nitrogen and charming properties such as highly porous nature, the void appearance in the layer, and thermal stability [36]. Initially, the computational studies reveal that functionalization of g-C₃N₄ by the Li ion leads to high specific capacity [37], and g-C₃N₄ nanotubes consisting of uniform pore size promote lithium storage [38]. In addition, the penetrating of Li ion is easier in such systems. Further, the electronic conductivity of the g-C₃N₄ is severely limited by the increasing concentration of g-C₃N₄, which subsequently decreases the storage capacity [39, 40]. When the C₃N₄ is lithiated, the metallic lithium reacts and devastates the crystallinity. Furthermore, various C₃N₄-based composite materials have been developed such as SnO₂-g-C₃N₄ which provides enhanced cyclic performance [41], the ternary composite SnS₂/g-C₃N₄/rGO gives a high lithium-ion diffusion coefficient, less interfacial resistance, and specific capacity of 1248 mAh g⁻¹ after 276 cycles [42]. The Fe₂O₃/C₃N₄/graphene-based anode shows excellent electrochemical behavior and large reversible capacity with high coulombic efficiency [43]. The 2D layered C₃N₄ sandwiched between the reduced graphene oxide exhibits a moderate capacity of 970 mAh g⁻¹ after 300 cycles [44]. However, despite the many advantages possessed by C₃N₄, the application of C₃N₄ is limited in LIB due to difficulty in Li-ion penetration into the porous electrode structure, deterioration of crystallinity, slow Li-ion intercalation/de-intercalation process, increasing the thickness of SEI, poor capacity, and cyclic stability. Therefore, we believe that there exists a wide possibility of enhancing the performance by tuning the physical and electrochemical properties of C₃N₄. Keeping this in mind, in this work, we have developed graphitic carbon nitride at different temperatures (500 °C, 600 °C) by using melamine as a precursor. Moreover, we expect that the calcination temperatures have significant impact over the surface area and stability of C₃N₄, which may assist in attaining enhanced electrochemical performance by providing a suitable electrochemical active site upon reacting with lithium ion from

the electrolyte. This may offer improved lithium-ion storage and enhance the rate of lithium-ion penetration into the porous electrode.

Experimental

Synthesis of C₃N₄ at different temperatures

Carbon nitride (C₃N₄) was obtained by direct heating of melamine (C₃N₆H₆) in a muffle furnace. The 10 g of melamine was loaded in an alumina crucible and calcined at 500 °C, 600 °C under nitrogen gas flow for 2 h with a heating rate of 2 °C/min. The obtained yellow powder was collected and washed with 0.1 M HNO₃ to remove the impurities [45–48].

Material characterization

A Fourier transform infrared spectrometer (FT-IR, Thermo Nicolet-600) was used to identify the functional group of the prepared material. To identify the phase purity and the crystalline structure of the sample, an X-ray diffractometer (model: X'Pert Pro) was used with a Cu K α radiation source ($\lambda K\alpha = 1.54060$). Thermal stability of the sample was identified using a thermogravimetric analyzer (TGA-DTA-Q600) with a heating rate 10 °C. A scanning electron microscope (FE-SEM, Carl Zeiss SUPRA55VP) and high-resolution transmission electron microscope (HR-TEM, TECNAI G2 20S-T WIN FEI) were used to identify the morphology of the sample. X-ray photoelectron spectroscopy (XPS) of the composite was performed using a PHI5000 versa probe spectrometer.

Electrochemical characterization

The electrochemical performance of the samples was tested using a CR2032-type coin cell. The working electrode was developed by mixing the active materials, super P carbon, and poly (vinylidene fluoride) (PVDF) with a weight ratio of 80:10:10% using N-methyl-2-pyrrolidone (NMP) as a solvent. The prepared slurry was uniformly coated on a copper foil and dried at 80 °C for 24 h in a vacuum oven. The electrode film was punched into 14-mm-diameter discs (area of 1.7 cm²) and weighed. The coin cells were assembled in an argon-filled glove box (M Braun). Commercially available LiPF₆ (1 M), dissolved in battery-grade ethylene carbonate/dimethyl carbonate, was used as an electrolyte and Celgard 2400 as a separator; then, the galvanostatic charge–discharge process and electrochemical impedance spectroscopy were performed on the coin cell and all the measurements were performed using a biologic multichannel battery workstation (VMP32) at room temperature.

Results and discussion

Figure 1a represents the FT-IR spectrum of the samples prepared at different temperatures, C_3N_4 -500 °C and C_3N_4 -600 °C. Both materials have similar features; a peak at 813 cm^{-1} indicates the characteristic breathing mode of triazine ring moieties [49]. The peaks at 1330 cm^{-1} and 1411 cm^{-1} belong to the symmetric stretching vibration mode of carbon nitride, and the peak at 1614 cm^{-1} corresponds to the asymmetric stretching vibration mode of the C–N that exists in the side chain [50]. The broadband that occurs between 3000 and 3500 cm^{-1} indicates that the presence of the N–H bond also indicates the O–H bond of surface absorbed water molecules. All the bands resembled the bands of pure C_3N_4 reported earlier [51, 52].

Raman spectra for the C_3N_4 synthesized at 500 °C and 600 °C are depicted in Fig. 1b. The peaks appearing at 356 cm^{-1} , 470 cm^{-1} , and 462 cm^{-1} indicate the vibrational

mode of the C–N heterocycle of C_3N_4 . The bands at 709 cm^{-1} , 771 cm^{-1} , and 979 cm^{-1} indicate the triazine ring. Further, the peaks at 1235 cm^{-1} and 1318 cm^{-1} confirm the presence of heterocyclic C–N and its analogs band [53]. Both C_3N_4 -500 °C and C_3N_4 -600 °C had similar Raman bands, but the intensity of C_3N_4 -600 °C increased as the processing temperature increased; this shows the presence of structural defects. The XRD patterns of the prepared C_3N_4 -500 °C and C_3N_4 -600 °C were identified using an X-ray diffractometer (model: X'Pert Pro) and illustrated in Fig. 1c. The samples consisting of two major diffraction peaks which appear at 27° indexed as the (002) plane. This indicates the two-dimensional hexagonal structure [54, 55], as well as the interplanar stacking of the existing aromatic system. The peak at 13° corresponds to the (100) plane. The above two peaks were consistent with the earlier-reported C_3N_4 [56]. Further, increasing the calcination temperature to 700 °C resulted in a complete decomposition of melamine and an empty crucible was observed. The

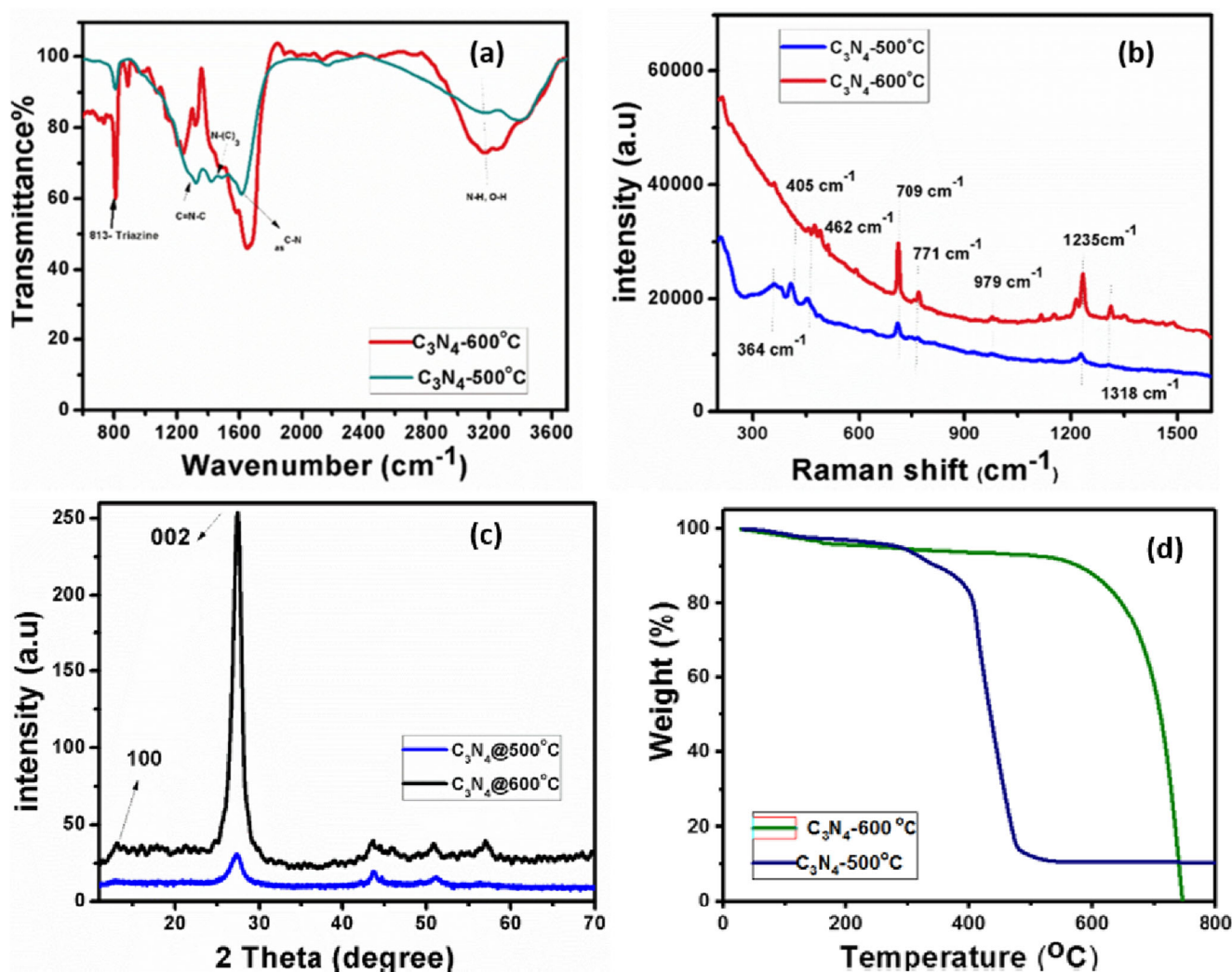


Fig. 1 a FT-IR spectra of C_3N_4 -500 °C and C_3N_4 -600 °C. b Raman spectra of C_3N_4 -500 °C and C_3N_4 -600 °C. c XRD pattern of C_3N_4 -500 °C and C_3N_4 -600 °C. d TGA data for C_3N_4 -500 °C and C_3N_4 -600 °C

thermal stability of the prepared C_3N_4 -500 °C and C_3N_4 -600 °C was investigated using a thermogravimetric analyzer under nitrogen flow and illustrated in Fig. 1d; for C_3N_4 -600 °C, a weight loss of 4% at 161 °C was observed due to the evaporation of water and volatile impurities. A weight loss of 2% corresponds to the existing terminal amine group decomposition that occurred between the temperatures of 162 and 312 °C, and C_3N_4 was found to be stable at a temperature of 547 °C which is provided by the existence of aromatic conjugation linked by carbon–nitrogen atoms [57]. The oxidative degradation of the C_3N_4 process leading to a weight loss of 82% occurred between the temperatures 529 and 740 °C. On further heating, the complete weight loss is finalized at 745 °C [58]. C_3N_4 -500 °C has similar features to C_3N_4 -600 °C and illustrated in Fig. 1d; the weight loss of 2.6% at 151–334 °C corresponds to the decomposition of terminal amine. From Fig. 1d, a rapid weight loss occurred from 335 to 481 °C due to oxidative degradation of carbon nitride. This thermal gravimetric analysis reveals that the thermal stability of C_3N_4 -500 °C is lower than that of C_3N_4 -600 °C.

The surface area and porous structure were measured by nitrogen adsorption/desorption isotherms using Brunauer–Emmet–Teller (BET, Quantachrome-ASiQwin, version 3.0) at 77 K and represented in Fig. 2. Both C_3N_4 -500 °C and C_3N_4 -600 °C shown in Fig. 2a have type IV adsorption–desorption isotherm with H3 hysteresis loops [49]. C_3N_4 -600 °C has a higher surface area (14.5 m²/g) than C_3N_4 -500 °C (surface area, 10.07 m²/g). The pore diameter of C_3N_4 -500 °C (23.36 nm) and C_3N_4 -600 °C (6.70 nm) shown in Fig. 2b, c indicates that C_3N_4 -500 °C and C_3N_4 -600 °C fall

on the mesoporous scale (i.e., pore size, 2–50 nm) [59–61]. This mesoporous feature is attributed to the capillary condensation causing the phenomenon of adsorption hysteresis, which is predominant in C_3N_4 -600 °C as compared to C_3N_4 -500 °C. The pore volume of C_3N_4 -500 °C (0.166 cm³ g^{−1}) is lesser than that of C_3N_4 -600 °C (0.23 cm³ g^{−1}). This shows that the adsorption of nitrogen is higher for C_3N_4 -600 °C in comparison with C_3N_4 -500 °C. These enhanced results are attributed to the formation of an extended triazine ring, which leads to enhanced active sites. Further, to understand the surface morphology and microstructure of C_3N_4 -500 °C and C_3N_4 -600 °C, SEM was used and the obtained micrographs are illustrated in Fig. 3. The image in Fig. 3a, b represents the SEM image of the sample prepared at 500 °C and shows an irregular aggregated granular type of structure [62]. In the case of C_3N_4 -600 °C, a disordered and an interlinked flake type of structure was observed, which is depicted in Fig. 3c, d). Further, a better understanding of the C_3N_4 -500 °C and C_3N_4 -600 °C microstructure was obtained using TEM analysis, and the results are represented in Fig. 3e–h.

To identify the chemical state and its chemical functionality, we carried out X-ray photoelectron spectroscopy (XPS) for C_3N_4 -600 °C only and presented the results in Fig. 4a–c. The survey spectra in Fig. 4a indicate the elemental composition and its binding energies as 288.2 (C 1s), 398.6 (N 1s), and 532.1 eV (O 1s). Figure 4b belongs to the C 1s spectra which have three peaks at 284.0 eV, 285.4 eV, and 287.8 eV corresponding to pure graphitic carbon C–C bond, sp² C atom bonded to nitrogen in an aromatic C=N system, and the carbon atom of N–C=N from the triazine moiety respectively

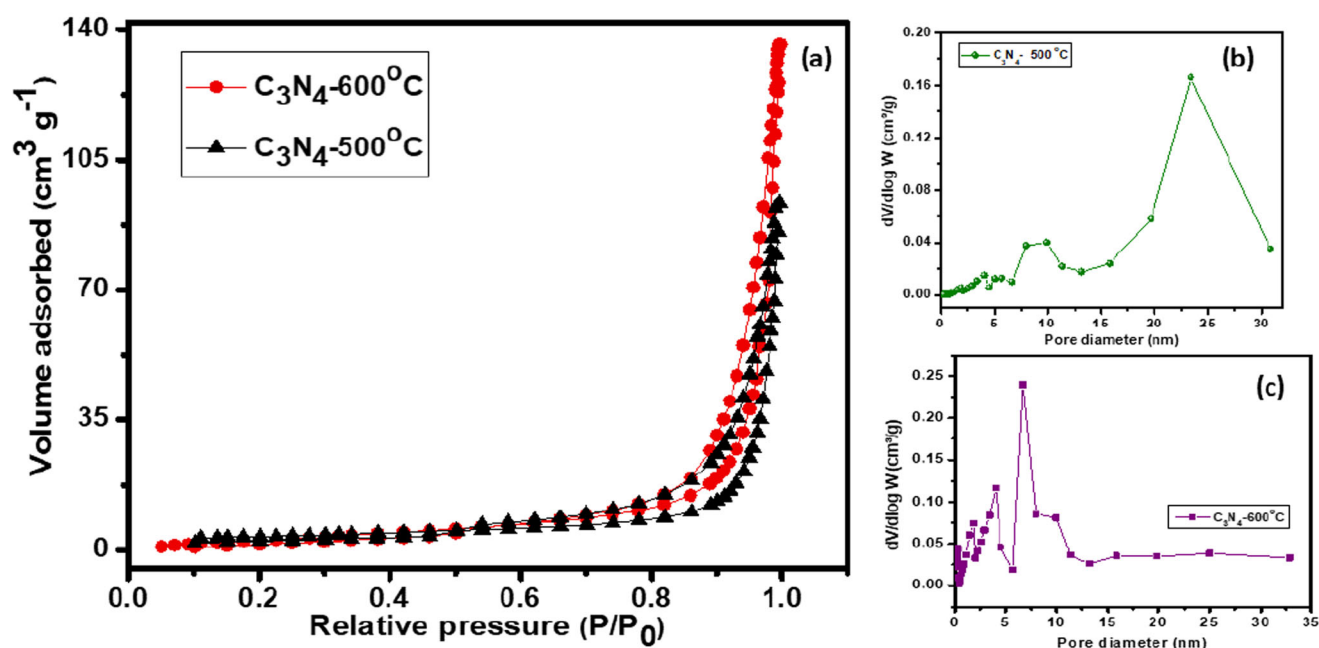


Fig. 2 a N_2 adsorption/desorption isotherms of C_3N_4 -500 °C and C_3N_4 -600 °C. b and c Pore size distribution of prepared C_3N_4 -500 °C and C_3N_4 -600 °C

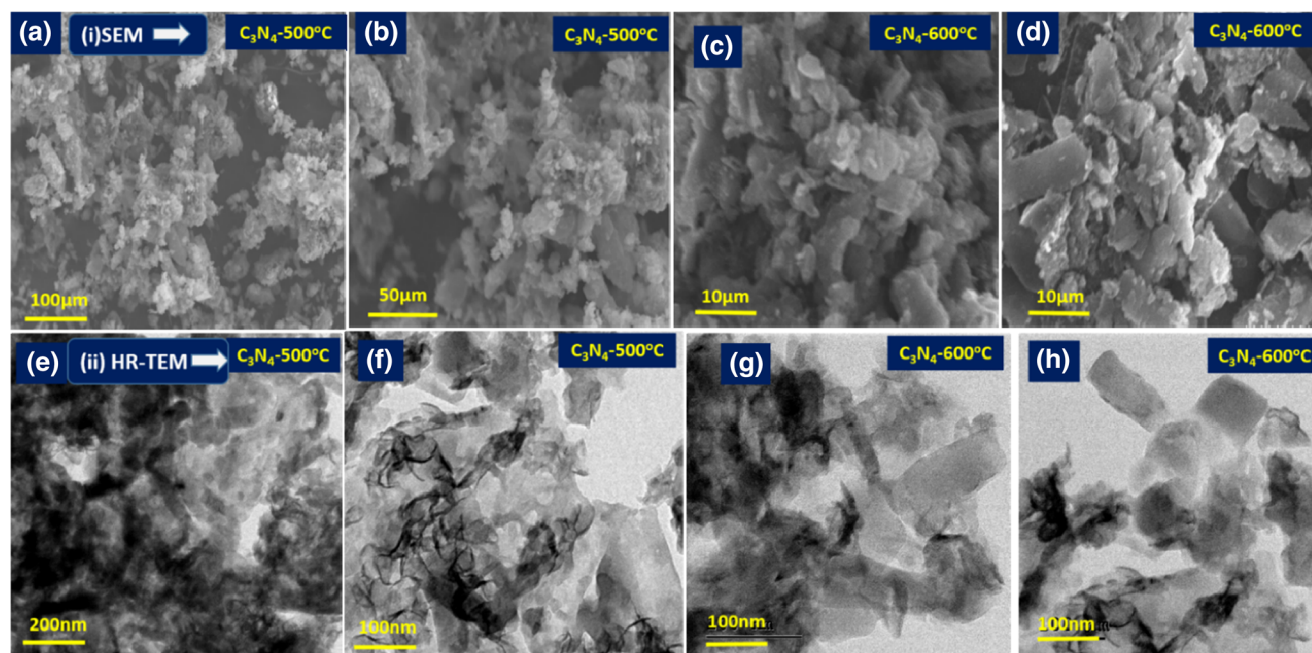


Fig. 3 i, SEM images of C_3N_4 -500 °C (a and b) and C_3N_4 -600 °C (c and d). ii, HR-TEM images of C_3N_4 -500 °C (e and f) and C_3N_4 -600 °C (g and h)

[63]. The N 1s spectrum in Fig. 4c is deconvoluted into three peaks at 398.1, 399.1, and 400.6 eV, corresponding to the sp^2 C–N=C, and Sp^3 N–(C)₃, and amino group C–N–H consisting of nitrogen bonded to H respectively [64].

The electrical conductivity measurements were carried out for the C_3N_4 synthesized at different temperatures (500 °C, 600 °C) using a SES instrument (model, DFP-RM-200). The prepared C_3N_4 at different temperatures (500 °C, 600 °C) was ground in a mortar and pestle, and pellets were made using a hydraulic pressure instrument. The thickness of the C_3N_4 -500 °C and C_3N_4 -600 °C pellets were 0.060 cm and 0.057 cm respectively. The electrical conductivity of the prepared pellets was measured using standard four-probe dc electrical conductivity-measuring techniques at room temperature. Colloidal silver paste was used to make contacts. The current–voltage data was generated (supplementary information), and the electrical conductivity was calculated using the following formula [65]:

$$\rho = \frac{\rho_0}{G_7 \left(\frac{W}{S} \right)} \quad (1)$$

where ρ_0 is uncorrected resistivity (ohm cm) and ρ is corrected resistivity; the correction factor $G_7(W/S)$ is used for the case of a non-conducting bottom surface, which is a function of thickness W (cm) and probe distance S (cm).

$$\rho_o = \frac{V}{I} \times 2\pi S \quad (2)$$

$$\sigma = \frac{1}{\rho} \quad (3)$$

Here, I is the current in amperes, V is the voltage, and σ is the dc electrical conductivity ($S\ cm^{-1}$).

In general, the electrical conductivity of semiconductor increases with increasing temperature [66–69]. Here, the electrical conductivity of C_3N_4 -500 °C and C_3N_4 -600 °C is about $1.463 \times 10^{-6} S\ cm^{-1}$ and $2.863 \times 10^{-6} S\ cm^{-1}$ respectively and shown in Tables 1 and 2. The enhanced electrical conductivity of C_3N_4 -600 °C is attributed to the existing conjugated triazine units bridged with N atom in the sp^2 configuration extending the π conjugation through the entire network. Furthermore, enhancing the process temperature of the material increases the crystalline quality, consisting of long range order and proper arrangement which leads to enhanced peak intensity. Also, short stacking distance between the layers and high degree of crystallization are in good agreement with XRD analysis. In addition to that, the natural defect of C_3N_4 -600 °C increases the electrical conductivity.

Electrochemical performances

The redox behavior of the prepared C_3N_4 -500 °C and C_3N_4 -600 °C was identified by cyclic voltammetry analysis and carried out between the potential ranges of 0 V to 3 V at a scan rate of 0.1 mV/s. Figure 5a indicates the cyclic voltammogram of C_3N_4 -500 °C; during the reductive sweep, C_3N_4 -500 °C shows a peak at +0.25 V which indicates the irreversible solid electrolyte interface (SEI) formation by electrolyte decomposition. [70]. The peak at +1.31 V indicates the insertion of Li ion to the active material and also represents the storage of Li ions. In the case of the anodic sweep, the delithiation process has appeared at +2.23 V [71]. In further

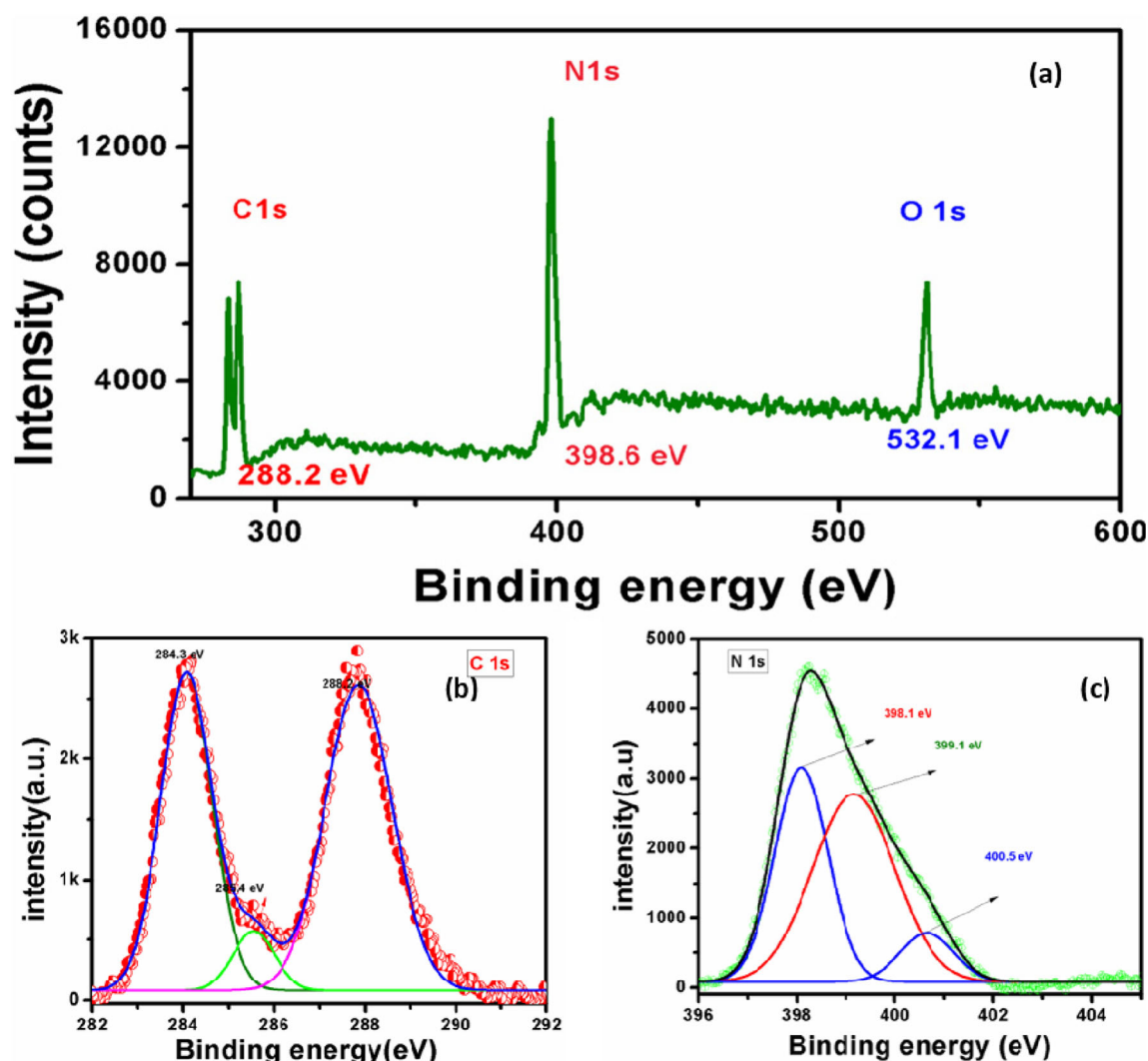


Fig. 4 X-ray photoelectron spectra of C_3N_4 -600 °C consisting of **a** survey, **b** C 1s, and **c** N 1s

cycles, the curves are overlapping each other; this reveals that the material has stable and superior reversibility. C_3N_4 -600 °C, shown in Fig. 5b, has similar features as observed in C_3N_4 -500 °C, but there is an increment in anodic and cathodic peak currents. This is attributed to the elevated temperature synthesis of C_3N_4 -600 °C which effectively enhances the condensation process as well as extends the triazine unit which

leads to enhanced π -conjugation. Also, this enhanced π -conjugation gives additional stability to the material.

To investigate the lithium storage capacity of C_3N_4 -500 °C and C_3N_4 -600 °C, galvanostatic discharge/charge measurements were employed at 0.1C. The discharge/charge capacities of the C_3N_4 -500 °C electrode for the 1st, 100th, 200th, and 300th cycles are 1680/961 mAh g⁻¹, 1506/839 mAh g⁻¹,

Table 1 Current (*I*)–voltage (*V*) data of C_3N_4 -500 °C

Electrical conductivity measurements of C_3N_4 -500 °C			
S. no.	Voltage (<i>V</i>)	Current (<i>I</i>) (μA)	<i>V/I</i> × 10 ⁶
01	0.01	0.004	2.5
02	0.02	0.008	2.5
03	0.03	0.012	2.5
04	0.04	0.016	2.5
Mean value = 2.5			

Table 2 Current (*I*)–voltage (*V*) data of C_3N_4 -600 °C

Electrical conductivity measurements of C_3N_4 -600 °C			
S. no.	Voltage (<i>V</i>)	Current (<i>I</i>) (μA)	<i>V/I</i> × 10 ⁶
01	0.01	0.011	0.9090
02	0.02	0.022	1.3636
03	0.03	0.033	1.5151
04	0.04	0.044	1.5909
Mean value = 1.346			

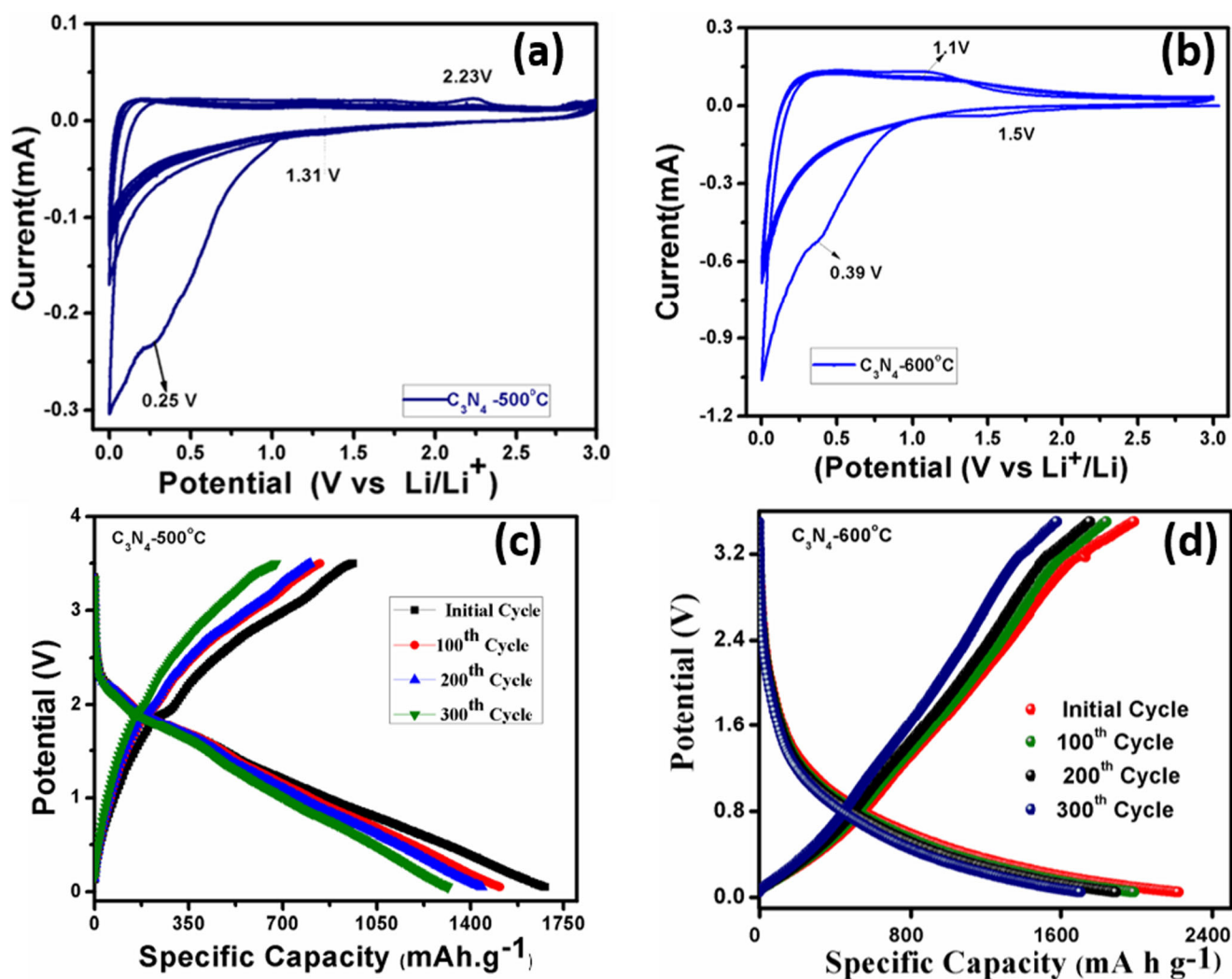


Fig. 5 a and b Cyclic voltammogram of C_3N_4 -500 °C and C_3N_4 -600 °C. c and d Charge–discharge voltage profile of C_3N_4 -500 °C and C_3N_4 -600 °C

1438/801 mAh g^{-1} , and 1313/673 mAh g^{-1} and represented in Fig. 5c. The discharge/charge capacity of C_3N_4 -600 °C is shown in Fig. 5d. The delivered discharge/charge capacity for the 1st, 100th, 200th, and 300th cycles are 2221/1986 mAh g^{-1} , 1986/1838 mAh g^{-1} , 1891/1751 mAh g^{-1} , and 1701/1576 mAh g^{-1} respectively. C_3N_4 -600 °C exhibits a high reversible capacity of 1701 mAh g^{-1} after 300 cycles, which is higher than C_3N_4 -500 °C.

The enhanced capacity observed may be due to the following characteristics: the high processing temperature synthesis increase in the triazine extension unit consisting of the conjugated π system. The tris-s-triazine units are connected by the planar amino groups which act as a template for the high lithium storage [72]. Also, the lithium ions tend to occupy the defects and nitrogen triangular holes of the C_3N_4 layers. The C_3N_4 consisting each nitrogen adsorb two Li atoms; the first lithium is attached to the void and the next lithium goes to the three nitrogen sites which leads to obtain the material with

high density of Li^+ ions; the expected reaction is $C_3N_4 + z\text{Li}^+ + ze^- = \text{Li}_zC_3N_4$ ($1 < z < 2$). This is in good agreement with earlier reports [73, 74]. In addition to that, C_3N_4 consists of a large number of uniform pores as well as reacts with lithium through Lewis–acid base interaction leading to the formation of a suitable solid electrolyte interface. Also, the high-interlinked structure with natural defect of C_3N_4 -600 °C provides access to store more lithium ions and creates diffusion channels, which shorten the diffusion of the Li-ion path and assists in a faster intercalation–de-intercalation process. Furthermore, enhancement in the electrochemical active porous site assists in increasing lithium-ion storage. Electrochemical impedance spectroscopy (EIS) was employed to investigate the resistance and kinetic behavior of C_3N_4 -500 °C and C_3N_4 -600 °C. The tests were recorded in the frequency range of 100 kHz–10 mHz with an excitation potential of 5 mV. The obtained data are presented in Fig. 6. Figure 6a indicates the Nyquist plot of before and after the charge/discharge process for C_3N_4 -500 °C. The Nyquist plots

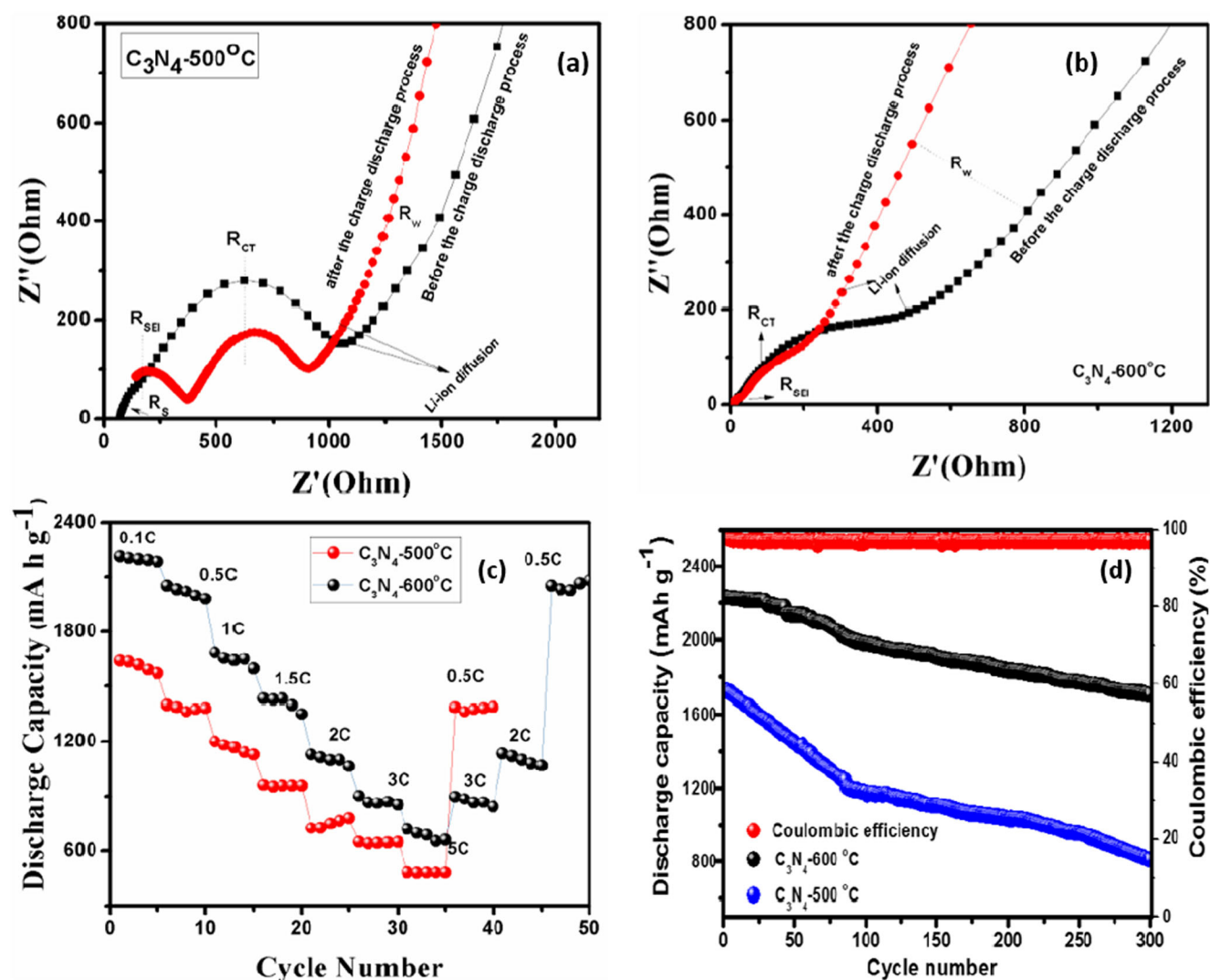


Fig. 6 **a** and **b** EIS-Nyquist plots of C_3N_4 -500 °C and C_3N_4 -600 °C before and after the charge–discharge process. **c** Rate capability of C_3N_4 -500 °C and C_3N_4 -600 °C. **d** Coulombic efficiency and cyclic stability of C_3N_4 -500 °C and C_3N_4 -600 °C

consist of electrode–electrolyte resistance (R_s), solid electrolyte interface resistance (R_{SEI}), charge transfer resistance (RCT), and Warburg impedance (R_w) due to ion diffusion into the active material. C_3N_4 -500 °C consists of two irregular semicircles. The first semi-circle is attributed to the formation of an irreversible solid electrolyte interface (SEI) at a high-frequency region, and the second semi-circle represents the double-layer capacity and charge transfer resistance at the electrodes, where the diffusion of lithium-ion domination occurs in the low-frequency region. After the charge–discharge process, the charge transfer resistance of C_3N_4 -500 °C was found to be less than that of the freshly assembled C_3N_4 -500 °C.

This is due to the high semiconducting nature and enhanced polarization due to various side reactions. Furthermore, the impedance analysis of the C_3N_4 -600 °C electrodes was carried out and presented in Fig. 6b. C_3N_4 -600 °C has a similar feature as C_3N_4 -500 °C. In comparison with

C_3N_4 -500 °C, the C_3N_4 -600 °C material exhibits a decrease in the charge resistance. This is obtained due to the uniform and high adsorption and distribution of Li ion on C_3N_4 -600 °C and formation of a suitable solid electrolyte interface and enhanced an electrochemical active site by the edge defect as well as possessing the suitable environment for binding and mobility of the lithium ion.

Figure 6c represents the rate capability of the prepared C_3N_4 -500 °C and C_3N_4 -600 °C under various current rates. Initially, the C_3N_4 -600 °C material displays a discharge capacity of 2207 mAh g⁻¹ at 0.1C. Further, cycling at 0.5C, 1C, 1.5C, 2C, 3C, and 5C the discharge capacity of 1980 mAh g⁻¹, 1597 mAh g⁻¹, 1409 mAh g⁻¹, 1099 mAh g⁻¹, 882 mAh g⁻¹, and 690 mAh g⁻¹ was observed. All the electrodes showed a decreasing discharge capacity with increasing C-rate. When the current density switched back from 5C to 0.5C, the initial discharge capacity of 2063 mAh g⁻¹ was largely recovered. This shows that

C_3N_4 -600 °C has a high rate capability and superior cyclic stability possessing high structural stability due to the presence of a high nitrogen content. Also, the structural defects of C_3N_4 -600 °C assist as well as act as a buffer medium in controlling volume expansion during the intercalation–de-intercalation process. The packing of C_3N_4 -600 °C is denser which is attributed to the enhanced π -conjugation. This is attained by the high-temperature synthesis that gives additional stability. Therefore, the above-mentioned results indicate that C_3N_4 -600 °C shows an enhanced rate due to electrochemical active consisting of transport channels, which makes the Li-ion penetration easier and faster. Figure 6 represents the comparison of cycling performance of C_3N_4 -500 °C and C_3N_4 -600 °C at 0.1C rate up to 300 cycles. C_3N_4 -600 °C initially delivers the discharge/charge capacity of 2221/1986 mAh g⁻¹ with 89% coulombic efficiency. After 300 cycles, the discharge capacity of 1701 mAh g⁻¹ was observed and a capacity retention of 92% was obtained. The observed discharge/charge capacity for C_3N_4 -500 °C is 1680/961 mAh g⁻¹ and an initial coulombic efficiency of 57% was obtained. C_3N_4 -600 °C shows higher capacity retention and better coulombic efficiency than C_3N_4 -500 °C. This is attributed to the active material activation as well as effective control in volume expansion during the charge–discharge process. In comparison with C_3N_4 -600 °C, the low capacity for C_3N_4 -500 °C may be attributed to the fact that the various irreversible side reactions between Li⁺ and the C_3N_4 lead to different products such as Li-CH=NR and Li=NCR₂ [40], which may increase the interfacial resistance and this may affect the mobility of ions.

Overall, the enhanced capacity, superior rate, and cyclic stability C_3N_4 -600 °C are attributed to the following characteristics: the elevated temperature synthesis assists in the development of the pure and crystallized disordered interlinked structure of C_3N_4 -600 °C having more active sites for the storage of Li ions. C_3N_4 -600 °C enlarges the contact area, when interacting with the electrolyte, as well as acts as a buffer medium in volume expansion during the charge–discharge process. This increases the electrochemical active surface area and provides a channel for fast lithium-ion transportation by reducing the ion transport distance. In addition, the enhanced surface area of C_3N_4 -600 °C paves the way for increased Li-ion storage and facilitates the redox kinetics.

Conclusion

In summary, we have discussed the electrochemical performance of synthesized carbon nitride at different temperatures (500 °C, 600 °C) by utilizing as anodes for LIB. The synthesized carbon nitride at 600 °C (C_3N_4 -600 °C) delivered an initial discharge/charge capacity of 2221/1986 mAh g⁻¹ with a reversible discharge capacity of 1701 mAh g⁻¹ after 300 cycles with superior rate and cyclic durability. This

outstanding electrochemical performance and structural features of C_3N_4 -600 °C widen the research possibilities for further development of carbon nitride-based electrode material for application in energy storage devices.

Acknowledgments The authors thank Pondicherry University for the financial support and central instrumentation facility (CIF).

Compliance with ethical standards

Conflict of interest The authors declare that they have no competing interests.

References

1. Lu L, Han X, Li J, Hua J, Ouyang M (2013) A review on the key issues for lithium-ion battery management in electric vehicles. *J Power Sources* 226:272–288. <https://doi.org/10.1016/j.jpowsour.2012.10.060>
2. Abada S, Marlair G, Lecocq A, Petit M, Sauvant-Moynot V, Huet F (2016) Safety focused modeling of lithium-ion batteries: a review. *J Power Sources* 306:178–192. <https://doi.org/10.1016/j.jpowsour.2015.11.100>
3. Bandhauer TM, Garimella S, Fuller TF (2011) A critical review of thermal issues in lithium-ion batteries. *J Electrochem Soc* 158:R1. <https://doi.org/10.1149/1.3515880>
4. Passerini S, Scrosati B (2016) Lithium and lithium-ion batteries: challenges and prospects. *Electrochem Soc Interface* 25:85. <https://doi.org/10.1149/2.F09163>
5. Peled E, Menkin S (2017) Review—SEI: past, present and future. *J Electrochem Soc* 164:A1703–A1719. <https://doi.org/10.1149/2.1441707jes>
6. An SJ, Li J, Daniel C, Mohanty D, Nagpure S, Wood DL III (2016) The state of understanding of the lithium-ion-battery graphite solid electrolyte interphase (SEI) and its relationship to formation cycling. *Carbon N Y* 105:52–76. <https://doi.org/10.1016/j.carbon.2016.04.008>
7. Szczech JR, Jin S (2011) Nanostructured silicon for high capacity lithium battery anodes. *Energy Environ Sci* 4:56–72. <https://doi.org/10.1039/C0EE00281J>
8. Chockla AM, Klavetter KC, Mullins CB, Korgel BA (2012) Solution-grown germanium nanowire anodes for lithium-ion batteries. *ACS Appl Mater Interfaces* 4:4658–4664. <https://doi.org/10.1021/am3010253>
9. Bruce PG, Scrosati B, Tarascon JM (2008) Nanomaterials for rechargeable lithium batteries. *Angew Chem Int Ed* 47:2930–2946. <https://doi.org/10.1002/anie.200702505>
10. Park C-M, Kim J-H, Kim H, Sohn H-J (2010) Li-alloy based anode materials for Li secondary batteries. *Chem Soc Rev* 39:3115–3141. <https://doi.org/10.1039/b919877f>
11. Wang Z, Zhou L, Lou XW (2012) Metal oxide hollow nanostructures for lithium-ion batteries. *Adv Mater* 24:1903–1911. <https://doi.org/10.1002/adma.201200469>
12. Yang J, Takeda Y, Imanishi N et al (2002) SiOx-based anodes for secondary lithium batteries. *Solid State Ionics* 152–153:125–129. [https://doi.org/10.1016/S0167-2738\(02\)00362-4](https://doi.org/10.1016/S0167-2738(02)00362-4)
13. Goriparti S, Miele E, De Angelis F et al (2014) Review on recent progress of nanostructured anode materials for Li-ion batteries. *J Power Sources* 257:421–443. <https://doi.org/10.1016/j.jpowsour.2013.11.103>
14. Yang J, Zhou XY, Li J, Zou YL, Tang JJ (2012) Study of nanoporous hard carbons as anode materials for lithium ion batteries.

- Mater Chem Phys 135:445–450. <https://doi.org/10.1016/j.matchemphys.2012.05.006>
15. Fujimoto H, Tokumitsu K, Mabuchi A, Chinnasamy N, Kasuh T (2010) The anode performance of the hard carbon for the lithium ion battery derived from the oxygen-containing aromatic precursors. *J Power Sources* 195:7452–7456. <https://doi.org/10.1016/j.jpowsour.2010.05.041>
 16. Nishidate K, Hasegawa M (2005) Energetics of lithium ion adsorption on defective carbon nanotubes. *Phys Rev B Condens Matter Mater Phys* 71:1–6. <https://doi.org/10.1103/PhysRevB.71.245418>
 17. Zhao J, Buldum A, Han J, Lu JP (2000) First-principles study of Li-intercalated carbon nanotube ropes. *Phys Rev Lett* 85:1706–1709. <https://doi.org/10.1103/PhysRevLett.85.1706>
 18. Meunier V, Kephart J, Roland C, Bernholc J (2002) Ab initio investigations of lithium diffusion in carbon nanotube systems. *Phys Rev Lett* 88:4. <https://doi.org/10.1103/PhysRevLett.88.075506>
 19. Schauerma CM, Ganter MJ, Gaustad G, Babbitt CW, Raffaele RP, Landi BJ (2012) Recycling single-wall carbon nanotube anodes from lithium ion batteries. *J Mater Chem* 22:12008. <https://doi.org/10.1039/c2jm31971c>
 20. Chen Z, Belharouak I, Sun YK, Amine K (2013) Titanium-based anode materials for safe lithium-ion batteries. *Adv Funct Mater* 23: 959–969. <https://doi.org/10.1002/adfm.201200698>
 21. Jiang J, Li Y, Liu J, Huang X, Yuan C, Lou XWD (2012) Recent advances in metal oxide-based electrode architecture design for electrochemical energy storage. *Adv Mater* 24:5166–5180. <https://doi.org/10.1002/adma.201202146>
 22. Lai C-H, Lu M-Y, Chen L-J (2012) Metal sulfide nanostructures: synthesis, properties and applications in energy conversion and storage. *J Mater Chem* 22:19–30. <https://doi.org/10.1039/C1JM13879K>
 23. Wang B, Chen JS, Bin WH et al (2011) Quasiemulsion-templated formation of ??-Fe₂O₃ hollow spheres with enhanced lithium storage properties. *J Am Chem Soc* 133:17146–17148. <https://doi.org/10.1021/ja208346s>
 24. Ding Z, Li X, Wei T, Yin Z, Li X (2016) Improved compatibility of graphite anode for lithium ion battery using sulfuric esters. *Electrochim Acta* 196:622–628. <https://doi.org/10.1016/j.electacta.2016.02.205>
 25. Wang C, Appleby AJ, Little FE (2001) Charge-discharge stability of graphite anodes for lithium-ion batteries. *J Electroanal Chem* 497:33–46. [https://doi.org/10.1016/S0022-0728\(00\)00447-2](https://doi.org/10.1016/S0022-0728(00)00447-2)
 26. Jeon Y, Noh HK, Song H-K (2017) A Lithium-ion battery using partially Lithiated graphite anode and Amphi-redox LiMn₂O₄ cathode. *Sci Rep* 7:14879. <https://doi.org/10.1038/s41598-017-14741-x>
 27. Liu C, Liu X, Tan J, Wang Q, Wen H, Zhang C (2017) Nitrogen-doped graphene by all-solid-state ball-milling graphite with urea as a high-power lithium ion battery anode. *J Power Sources* 342:157–164. <https://doi.org/10.1016/j.jpowsour.2016.11.110>
 28. Zhang J, Li C, Peng Z, Liu Y, Zhang J, Liu Z, Li D (2017) 3D free-standing nitrogen-doped reduced graphene oxide aerogel as anode material for sodium ion batteries with enhanced sodium storage. *Sci Rep* 7:1–7. <https://doi.org/10.1038/s41598-017-04958-1>
 29. Cheng Q, Okamoto Y, Tamura N, Tsuji M, Maruyama S, Matsuo Y (2017) Graphene-like-graphite as fast-chargeable and high-capacity anode materials for lithium ion batteries. *Sci Rep* 7:1–14. <https://doi.org/10.1038/s41598-017-14504-8>
 30. Jiang M-H (2017) Nitrogen-doped graphene sheets prepared from different graphene-based precursors as high capacity anode materials for lithium-ion batteries. *Int J Electrochem Sci* 12:7154–7165. <https://doi.org/10.20964/2017.08.14>
 31. Xiong D, Li X, Bai Z, Shan H, Fan L, Wu C, Li D, Lu S (2017) Superior cathode performance of nitrogen-doped graphene frameworks for lithium ion batteries. *ACS Appl Mater Interfaces* 9: 10643–10651. <https://doi.org/10.1021/acsami.6b15872>
 32. Liu X, Liu E, Chao D, Chen L, Liu S, Wang J, Li Y, Zhao J, Kang YM, Shen Z (2016) Large size nitrogen-doped graphene-coated graphite for high performance lithium-ion battery anode. *RSC Adv* 6:104010–104015. <https://doi.org/10.1039/C6RA23228K>
 33. Yuan G, Xiang J, Jin H, Wu L, Jin Y, Zhao Y (2018) Anchoring ZnO nanoparticles in nitrogen-doped graphene sheets as a high-performance anode material for lithium-ion batteries. *Materials (Basel)* 11:15–17. <https://doi.org/10.3390/ma11010096>
 34. Hu J, Tian J, Li C (2017) Nanostructured carbon nitride polymer-reinforced electrolyte to enable dendrite-suppressed lithium metal batteries. *ACS Appl Mater Interfaces* 9:11615–11625. <https://doi.org/10.1021/acsami.7b00478>
 35. Wang Y, Wang X, Antonietti M (2012) Polymeric graphitic carbon nitride as a heterogeneous organocatalyst: from photochemistry to multipurpose catalysis to sustainable chemistry. *Angew Chem Int Ed* 51:68–89. <https://doi.org/10.1002/anie.201101182>
 36. Zhao Z, Sun Y, Dong F (2015) Graphitic carbon nitride based nanocomposites: a review. *Nanoscale* 7:15–37. <https://doi.org/10.1039/C4NR03008G>
 37. Wu M, Wang Q, Sun Q, Jena P (2013) Functionalized graphitic carbon nitride for efficient energy storage. *PDF. J Phys Chem C* 117: 6055–6059. <https://doi.org/10.1021/jp311972f>
 38. Pan H (2014) Graphitic carbon nitride nanotubes as Li-ion battery materials: a first-principles study. *J Phys Chem C* 118:9318–9323. <https://doi.org/10.1021/jp4122722>
 39. Miller TS, Jorge AB, Sella A, Corà F, Shearing PR, Brett DJL, McMillan PF (2015) The use of graphitic carbon nitride based composite anodes for lithium-ion battery applications. *Electroanalysis*. 27:2614–2619. <https://doi.org/10.1002/elan.201500205>
 40. Veith GM, Baggetto L, Adamczyk LA, Guo B, Brown SS, Sun XG, Albert AA, Humble JR, Barnes CE, Bojdy MJ, Dai S, Dudney NJ (2013) Electrochemical and solid-state lithiation of graphitic C₃N₄. *Chem Mater* 25:503–508. <https://doi.org/10.1021/cm303870x>
 41. Vo V, Dieu X, Thi N et al (2017) SnO₂ nanosheets/g-C₃N₄ composite with improved lithium storage capabilities. *Chem Phys Lett* 674:42–47. <https://doi.org/10.1016/j.cplett.2017.02.057>
 42. Sher Shah MSA, Park AR, Rauf A, Hong SH, Choi Y, Park J, Kim J, Kim WJ, Yoo PJ (2017) Highly interdigitated and porous architected ternary composite of SnS₂, g-C₃N₄, and reduced graphene oxide (rGO) as high performance lithium ion battery anodes. *RSC Adv* 7:3125–3135. <https://doi.org/10.1039/C6RA25886G>
 43. Shi M, Wu T, Song X, Liu J, Zhao L, Zhang P, Gao L (2016) Active Fe₂O₃ nanoparticles encapsulated in porous g-C₃N₄/graphene sandwich-type nanosheets as a superior anode for high-performance lithium-ion batteries. *J Mater Chem A* 4:10666–10672. <https://doi.org/10.1039/C6TA03533G>
 44. Subramaniyam CM, Deshmukh KA, Tai Z et al (2017) 2D layered graphitic carbon nitride sandwiched with reduced graphene oxide as nanoarchitected anode for highly stable lithium-ion battery. *Electrochim Acta* 237:69–77. <https://doi.org/10.1016/j.electacta.2017.03.194>
 45. Hatamie A, Marahel F, Sharifat A (2018) Green synthesis of graphitic carbon nitride nanosheet (g-C₃N₄) and using it as a label-free fluorosensor for detection of metronidazole via quenching of the fluorescence. *Talanta* 176:518–525. <https://doi.org/10.1016/j.talanta.2017.08.059>
 46. Thomas A, Fischer A, Goettmann F, Antonietti M, Müller JO, Schlögl R, Carlsson JM (2008) Graphitic carbon nitride materials: variation of structure and morphology and their use as metal-free catalysts. *J Mater Chem* 18:4893. <https://doi.org/10.1039/b800274f>
 47. Xu J, Li Y, Peng S, Lu G, Li S (2013) Eosin Y-sensitized graphitic carbon nitride fabricated by heating urea for visible light photocatalytic hydrogen evolution: the effect of the pyrolysis temperature of

- urea. *Phys Chem Chem Phys* 15:7657–7665. <https://doi.org/10.1039/c3cp44687e>
48. Yin Y, Han J, Zhang X, Zhang Y, Zhou J, Muir D, Sutarto R, Zhang Z, Liu S, Song B (2014) Facile synthesis of few-layer-thick carbon nitride nanosheets by liquid ammonia-assisted lithiation method and their photocatalytic redox properties. *RSC Adv* 4:32690–32697. <https://doi.org/10.1039/C4RA06036A>
 49. Cao Y, Li Q, Wang W (2017) Construction of a crossed-layer-structure MoS₂/g-C₃N₄ heterojunction with enhanced photocatalytic performance. *RSC Adv* 7:6131–6139. <https://doi.org/10.1039/C6RA26925G>
 50. Fu X, Hu X, Yan Z, Lei K, Li F, Cheng F, Chen J (2016) Template-free synthesis of porous graphitic carbon nitride/carbon composite spheres for electrocatalytic oxygen reduction reaction. *Chem Commun* 52:1725–1728. <https://doi.org/10.1039/c5cc08897f>
 51. Zhao H, Dong Y, Jiang P, Miao H, Wang G, Zhang J (2015) In situ light-assisted preparation of MoS₂ on graphitic C₃N₄ nanosheets for enhanced photocatalytic H₂ production from water. *J Mater Chem A* 3:7375–7381. <https://doi.org/10.1039/c5ta00402k>
 52. Angamuthu G, Babu DB, Ramesha K, Rangarajan V (2019) MoS₂ anchored carbon nitride based mesoporous material as a polysulfide barrier for high capacity lithium-sulfur battery. *J Electroanal Chem* 843:37–46. <https://doi.org/10.1016/j.jelechem.2019.05.006>
 53. Praus P, Svoboda L, Ritz M, Troppová I, Šihor M, Kočí K (2017) Graphitic carbon nitride: synthesis, characterization and photocatalytic decomposition of nitrous oxide. *Mater Chem Phys* 193:438–446. <https://doi.org/10.1016/j.matchemphys.2017.03.008>
 54. Li X, Zhang J, Shen L, Ma Y, Lei W, Cui Q, Zou G (2009) Preparation and characterization of graphitic carbon nitride through pyrolysis of melamine. *Appl Phys A Mater Sci Process* 94:387–392. <https://doi.org/10.1007/s00339-008-4816-4>
 55. Sun B, Yu H, Yang Y, Li HJ, Zhai CY, Qian DJ, Chen M (2017) New complete assignment of X-ray powder diffraction patterns in graphitic carbon nitride using discrete Fourier transform and direct experimental evidence. *Phys Chem Chem Phys* 19:26072–26084. <https://doi.org/10.1039/C7CP05242A>
 56. Lan Y, Li Z, Li D, Yan G, Yang Z, Guo S (2019) Graphitic carbon nitride synthesized at different temperatures for enhanced visible-light photodegradation of 2-naphthol. *Appl Surf Sci* 467–468:411–422. <https://doi.org/10.1016/j.apsusc.2018.10.152>
 57. Cui Y, Zhang J, Zhang G, Huang J, Liu P, Antonietti M, Wang X (2011) Synthesis of bulk and nanoporous carbon nitride polymers from ammonium thiocyanate for photocatalytic hydrogen evolution. *J Mater Chem* 21:13032. <https://doi.org/10.1039/c1jm11961c>
 58. Huang Z, Yan FW, Yuan G (2017) A fluorescent carbon nitride nanofibrous hydrogel for selective sensing of Cu²⁺. *RSC Adv* 7:1318–1325. <https://doi.org/10.1039/c6ra26136a>
 59. Thommes M, Kaneko K, Neimark AV, Olivier JP, Rodriguez-Reinoso F, Rouquerol J, Sing KSW (2015) Physisorption of gases, with special reference to the evaluation of surface area and pore size distribution (IUPAC technical report). *Pure Appl Chem* 87:1051–1069. <https://doi.org/10.1515/pac-2014-1117>
 60. Maeda K, Kuriki R, Zhang M, Wang X, Ishitani O (2014) The effect of the pore-wall structure of carbon nitride on photocatalytic CO₂ reduction under visible light. *J Mater Chem A* 2:15146–15151. <https://doi.org/10.1039/c4ta03128h>
 61. Störck S, Brettinger H, Maier WF (1998) Characterization of micro- and mesoporous solids by physisorption methods and pore-size analysis. *Appl Catal A Gen* 174:137–146. [https://doi.org/10.1016/S0926-860X\(98\)00164-1](https://doi.org/10.1016/S0926-860X(98)00164-1)
 62. Zhang Y, Pan Q, Chai G, Liang M, Dong G, Zhang Q, Qiu J (2013) Synthesis and luminescence mechanism of multicolor-emitting g-C₃N₄ nanopowders by low temperature thermal condensation of melamine. *Sci Rep* 3:1–8. <https://doi.org/10.1038/srep01943>
 63. Wang X, Hong M, Zhang F, Zhuang Z, Yu Y (2016) Recyclable nanoscale zero valent iron doped g-C₃N₄/MoS₂ for efficient photocatalysis of RhB and Cr(VI) driven by visible light. *ACS Sustain Chem Eng* 4:4055–4063. <https://doi.org/10.1021/acsschemeng.6b01024>
 64. Xiang Q, Yu J, Jaroniec M (2011) Preparation and enhanced visible-light photocatalytic H₂-production activity of graphene/C₃N₄ composites. *J Phys Chem C* 115:7355–7363. <https://doi.org/10.1021/jp200953k>
 65. Khan A, Khan AAP, Asiri AM, Rub MA, Azum N, Khan I (2014) Preparation, electrical conductivity, and thermal studies on silver doped polyaniline phosphotungstate nanocomposite. *Synth React Inorganic Met Nano-Metal Chem* 44:1526–1530. <https://doi.org/10.1080/15533174.2013.802334>
 66. Kim JI, Kang PH, Nho YC (2004) Positive temperature coefficient behavior of polymer composites having a high melting temperature. *J Appl Polym Sci* 92:394–401. <https://doi.org/10.1002/app.20064>
 67. Buerschaper RA (1944) Thermal and electrical conductivity of graphite and carbon at low temperatures. *J Appl Phys* 15:452–454. <https://doi.org/10.1063/1.1707454>
 68. Fang XY, Yu XX, Zheng HM, Jin HB, Wang L, Cao MS (2015) Temperature- and thickness-dependent electrical conductivity of few-layer graphene and graphene nanosheets. *Phys Lett Sect A Gen Solid State Phys* 379:2245–2251. <https://doi.org/10.1016/j.physleta.2015.06.063>
 69. Ioannou M, Polymeris G, Hatzikraniotis E et al (2013) Solid-state synthesis and thermoelectric properties of Sb-Doped Mg₂Si materials. *J Electron Mater* 42:1827–1834. <https://doi.org/10.1007/s11664-012-2442-6>
 70. Chenrayan S, Chandra K, Manickam S (2017) Ultrathin MoS₂ sheets supported on N-rich carbon nitride nanospheres with enhanced lithium storage properties. *Appl Surf Sci* 410:215–224. <https://doi.org/10.1016/j.apsusc.2017.03.102>
 71. Chen J, Mao Z, Zhang L, Wang D, Xu R, Bie L, Fahlman BD (2017) Nitrogen-deficient graphitic carbon nitride with enhanced performance for lithium ion battery anodes. *ACS Nano* 11:12650–12657. <https://doi.org/10.1021/acsnano.7b07116>
 72. Fu Y, Zhu J, Hu C, Wu X, Wang X (2014) Covalently coupled hybrid of graphitic carbon nitride with reduced graphene oxide as a superior performance lithium-ion battery anode. *Nanoscale* 6:12555–12564. <https://doi.org/10.1039/c4nr03145h>
 73. Guo Y, Niu P, Liu Y, Ouyang Y, Li D, Zhai T, Li H, Cui Y (2019) An autotransferable g-C₃N₄ Li⁺-modulating layer toward stable lithium anodes. *Adv Mater* 31:1–10. <https://doi.org/10.1002/adma.201900342>
 74. Weng GM, Xie Y, Wang H, Karpovich C, Lipton J, Zhu J, Kong J, Pfefferle LD, Taylor AD (2019) A promising carbon/g-C₃N₄ composite negative electrode for a long-life sodium-ion battery. *Angew Chem Int Ed* 58:13727–13733. <https://doi.org/10.1002/anie.201905803>